Inorganic Chemistry

Article

pubs.acs.org/IC

$BaMn_9[VO_4]_6(OH)_2$: A Unique Canted Antiferromagnet with a Chiral "Paddle-Wheel" Structural Feature

Kewen Sun,[†] Alexander P. Litvinchuk,[‡] Joshua Tapp,[†] Bernd Lorenz,[‡] and Angela Möller*[,†]

[†]Department of Chemistry and Texas Center for Superconductivity, University of Houston, Houston, Texas 77204-5003, United States

[‡]Department of Physics and Texas Center for Superconductivity, University of Houston, Houston, Texas 77204-5002, United States

Supporting Information

ABSTRACT: $BaMn_9[VO_4]_6(OH)_2$ was synthesized by hydrothermal methods. We evaluated the crystal structure based on the two possible space groups $P2_13$ and $Pa\bar{3}$ [a = 12.8417(2) Å] using single-crystal and powder X-ray diffraction techniques. The structure contains three-dimensionally linked Mn_9 units of a chiral "paddle-wheel" type. Experimental IR and Raman spectra were analyzed in terms of fundamental vanadate and hydroxide vibrational modes. The magnetic properties were investigated, and the specific heat in applied fields was studied. The dominant magnetic interactions (Mn^{2+}, $S = {}^5/_2$) are of antiferromagnetic origin, as indicated by a Curie–Weiss fit above 175 K with $\Theta \approx -200$ K. Canting of the spins on the geometrically frustrated triangle segment of the structural feature is considered to account for the ferrimagnetic type of long-range order at $T_C \approx 18$ K. We propose a model for the spin structure in the ordered regime. Dielectric constants were measured and indicate a magnetodielectric effect at T_C, which is assigned to spin–lattice coupling.

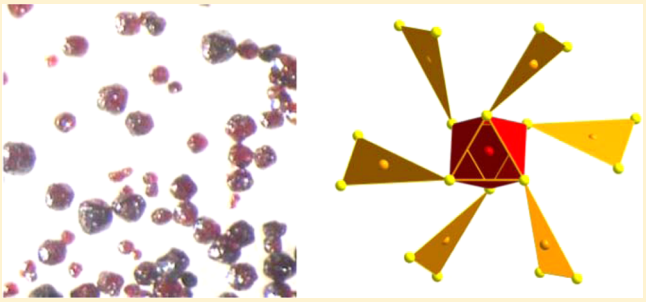

INTRODUCTION

Current research efforts are geared toward finding unusual magnetic materials with unique structural features that can lead to novel insights into structure–property relationships. Among these materials, special interest is given to those that exhibit coupling of the magnetic order to the electric polarization. Materials of this class are classified as multiferroics.[1−4] As more theoretical work is developed, certain characteristics have become available to guide an exploratory solid-state approach.[3] It has been found that multiferroicity might occur for compounds with magnetically induced ferroelectricity.[1] Examples are $CaBaCo_4O_7$ (noncollinear ferrimagnet),[5] $RbFe(MoO_4)_2$ or $AAg_2Fe[VO_4]_2$ with A = K or Rb (120° chiral and helical magnetic order),[6,7] and Cu_2OSeO_3 (skyrmion phase).[8]

An important ingredient for multiferroicity is the so-called geometrical frustration, which might occur in antiferromagnets with restrained equilateral triangles. This requires the preservation of 3-fold symmetry. Another aspect is the presence of a large magnetic moment per ion without significant spin–orbit coupling, such as Mn^{2+} or Fe^{3+} with $S = {}^5/_2$.[3,4] With these limitations in mind, we selected $BaMn_9[VO_4]_6(OH)_2$ as a presumably unique compound for our studies on novel magnetic materials with potential magnetodielectric coupling or even multiferroic properties. Previously, only the structure of the mineral nabiasite, $BaMn_9[(V,As)O_4]_6(OH)_2$, was reported.[9] We have synthesized the synthetic vanadate by hydrothermal methods, redetermined the crystal structure, and investigated the spectroscopic, magnetic, and dielectric properties.

It is worth mentioning that the number of structurally known compounds within the chemical phase diagram Ba^{2+}–Mn^{2+}–VO_4^{3-}–OH^- is rather limited. Examples are $BaMn_2[VO_4]_2$[10] or $BaAg_2Mn[VO_4]_2$[11] and $Mn_{7-2/3z}(OH)_3(VO_4)_{4-2z}(V_2O_7)_z$ with $z \approx 0.199(3)$,[12] $Mn_2(OH)[VO_4]$,[13] or $PbMn[VO_4](OH)$.[14] Thus, $BaMn_9[VO_4]_6(OH)_2$ stands out in two ways. To the best of our knowledge, this compound contains the largest number of magnetic ions per formula unit in combination with mixed anions, namely, vanadate and hydroxide. Our research efforts have also been motivated by the Mn-rich compound $CaMn_7O_{12}$. This perovskite-type material has recently received much attention because of the discovery of its giant polarization and magnetoorbital helices.[15]

EXPERIMENTAL SECTION

Synthesis. Dark-red crystals of $BaMn_9[VO_4]_6(OH)_2$ were synthesized by hydrothermal methods using 59 mg of NH_4VO_3 (ICN Pharmaceuticals, Inc.), 94 mg of $MnCl_2$ (Aldrich), 128 mg of $Ba(Ac)_2$ (Strem Chemicals), and 106 mg of LiCl (J. T. Baker Chemical Co.) as starting materials in a molar ratio of 1:1.5:1:5. After 10 mL of distilled water was added to the starting materials, drops of concentrated $NH_3 \cdot H_2O$ (14.8 M, EMD) were used to adjust the pH to 8.0. The total volume of the reaction mixture was loaded into a 12 mL Teflon-lined stainless steel autoclave. The reactions were kept in the furnace for 3–4

Special Issue: To Honor the Memory of Prof. John D. Corbett

Received: September 17, 2014
Published: November 19, 2014

   dx.doi.org/10.1021/ic502266k | Inorg. Chem. 2015, 54, 898–904

days at a typical temperature of 220 °C, then cooled to 120 °C at 6 °C/h, and finally to room temperature within 3 h. The final pH of the mother liquid dropped below 4, indicating that the crystalline product contains hydroxide. The crystals were collected by filtering, washed several times with distilled water, and dried naturally in the hood. Typical yields were ≈55% based on Mn. The crystalline product is shown in Figure 1. The

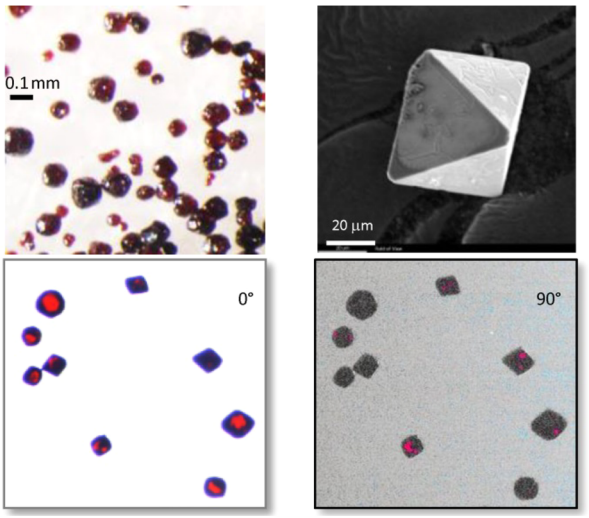

Figure 1. Top: Microscopic picture (left) and SEM picture of a C-coated crystal (right) of $BaMn_9[VO_4]_6(OH)_2$. Below: Polarized microscopic pictures of arbitrarily oriented crystals. For better contrast, the background in 90° polarization has been modified (brighter gray shade instead of black).

diameter of block-shaped crystals is approximately 0.1 mm on average. An Olympus BX 41-P polarizing microscope equipped with an Olympus DP12 microscope digital camera system was used. Note that for a cubic centrosymmetric structure no polarization is expected; thus, complete extinction in cross-polarized light (denoted as 90°) results. However, the observation of weak "red spots" on certain crystal faces (90° polarization) points toward a polar (acentric) space group.

Chemical Analysis. Coating of the sample with a thin film of carbon (approximately 250 Å thickness) was performed in a vacuum at 9.5×10^{-5} Torr using a Ladd Research Industries carbon evaporator. Scanning electron microscopy (SEM) data were recorded on a Jeol JSM 8330 F scanning electron microscope equipped with an energy-dispersive spectrometer using a silicon drift X-ray detector by means of a 15 kV accelerating voltage and a 12 µA emission current from a cold-field emission gun. The SEM picture shows the octahedral shape of a C-coated crystal; see Figure 1. The composition was confirmed by energy-dispersive spectrometry (EDS) analysis; average values from 22 measured spots: 1.0(1) for Ba, 5.8(2) for V, and 9.2(4) for Mn.

Structure Determination. A single-crystal data set was collected on an APEX II CCD detector from Bruker AXS Instruments (Mo Kα radiation with λ = 0.71073 Å) at room temperature. The unit cell parameters were determined using the program *SAINT*,[16] and the structure was solved by direct methods and refined by difference Fourier synthesis (program system *SHELX-2013*).[17] An absorption correction was applied using *MULTISCAN*,[18] implemented in the *WinGX* platform.[19] The structure was refined in the space groups $P2_13$ and $Pa\bar{3}$, respectively, using the AFIX 3 command and the ride-on constraint $U_{iso}(H) = -1.5U_{aniso}(O)$ for the H atoms. For the refinement in $P2_13$, the temperature factors of (pseudo)symmetry-related atoms were coupled (EADP command) to minimize correlation effects. Thus, only 87 out of 127 possible parameters were refined independently. Note that the absolute structure cannot be determined reliably, the Flack parameter x = 0.49(8), and alternative refinement as a two-component twinned structure gives 0.5(1). Crystallographic data for $BaMn_9[VO_4]_6(OH)_2$ are included in Table 1 and the Supporting Information (SI). The program *Diamond*[20] was used to illustrate the crystal structure.

Table 1. Crystallographic Data for $BaMn_9[VO_4]_6(OH)_2$

formula	$BaH_2Mn_9O_{26}V_6$	
fw (g/mol)	1355.46	
T (K)	293	
cryst syst	cubic	
space group	$Pa\bar{3}$ (No. 205)	$P2_13$ (No. 198)
a (Å)	12.8417(2)	
V (Å^3)	2117.7(1)	
Z	4	
D_{cal} (Mg/m^3)	4.251	
F_{000}	2516	
μ (mm^{-1})	9.61	
Θ_{max} (deg)	28.3	
ranges	$-17 \le h \le 13, -16 \le k \le 17, -14 \le l \le 17$	
no. of total,	11735	11735
rejected, and	807	none
unique reflns	891	1775
R_{int}	0.044	
no. of obsd reflns [$I > 2\sigma(I)$]	846	1555
no. of param	65	87
R1 [$I > 2\sigma(I)$]	0.018	0.022
wR2 [all data]	0.050	0.063
GOF	1.25	1.15
largest diff peak, hole (e/Å^3)	0.38, −1.69	0.49, −1.23

A PANalytical X'Pert Pro diffractometer (with λ Cu Kα_1 = 1.540562 Å and Kα_2 = 1.544389 Å) was used to collect diffraction patterns to confirm the phase purity and the structure model of the products. Samples were ground into fine powders and placed on a PW1817/32 zero-background silicon crystal sample holder. Lattice constants were refined by profile-matching (LeBail fit) methods using the program *Fullprof*.[21] Powder refinement data for $BaMn_9[VO_4]_6(OH)_2$ [a = 12.83629(5) Å, χ^2 = 3.31, Bragg R factor = 2.26, and R_f factor = 1.96 for $P2_13$, and a = 12.83624(5) Å, χ^2 = 3.23, Bragg R factor = 2.42, and R_f factor = 2.24 for $Pa\bar{3}$] are shown in Figure 2.

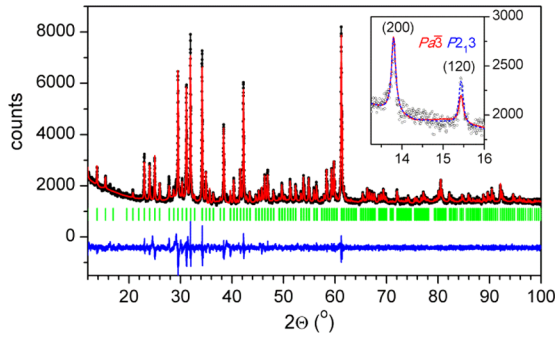

Figure 2. Powder refinement data for $BaMn_9[VO_4]_6(OH)_2$: observed (black); calculated (red); Bragg positions (green); difference (blue). Inset: Difference in the calculated intensities for the (120) reflection. Experimental data are given as black circles.

Property Measurements. $BaMn_9[VO_4]_6(OH)_2$ has been studied by spectroscopic methods. IR spectra were collected in an argon-filled glovebox on an Alpha-P IR spectrometer (Bruker) in reflectance mode. Raman (RA) spectra were recorded in the backscattering geometry on a single crystal using a Horiba Jobin Yvon T 6400 spectrometer with an optical microscope, a liquid-nitrogen-cooled CCD detector, and a laser excitation of Ar^+ (λ = 514.5 nm, 2.41 eV). The experimental resolution

dx.doi.org/10.1021/ic502266k | Inorg. Chem. 2015, 54, 898−904

did not exceed 1.5 cm^{-1}. The crystal was oriented with a trigonal face aligned perpendicular to the incident beam.

Magnetic and specific heat measurements were carried out on a Physical Property Measurement System (Quantum Design) from 2 to 300 K in applied fields up to 8 T. Susceptibility data were obtained in field-cooled (fc) and zero-field-cooled (zfc) modes and corrected for diamagnetic contributions.

Dielectric constants were measured on pressed powder pellets from 2 to 50 K using the high-precision capacitance bridge AH 2500A (Andeen-Hagerling) operating at a frequency of 1000 Hz. The capacitance was measured between two contacts made of silver paint attached to parallel faces of the pellet.

Calculations. First-principles calculations of the electronic ground state were performed within the generalized gradient approximation using Perdew–Burke–Ernzerhof local functional,[22] as implemented in the *CASTEP* code.[23] Norm-conserving pseudopotentials were used. The structure was relaxed for the experimentally determined lattice parameters, so that forces on atoms in the equilibrium position did not exceed 3 meV/Å.

RESULTS

Crystal Structure. Crystallographic data are listed in Table 1. $BaMn_9[VO_4]_6(OH)_2$ crystallizes in the cubic space group $P2_13$ or $Pa\bar{3}$. Our single-crystal data indicate that 18 reflections $[\sigma(F_o^2) \approx 5]$ of the type $0kl$ with $k = 2n$ violate the systematic absence requirements for $Pa\bar{3}$. However, we solved the structure in $P2_13$ and then applied the program system *PLATON*.[24] Within the range of deviations in distances and angles (e.g., 0.25° in angles), the space group $Pa\bar{3}$ is suggested and indicates possible pseudosymmetry.

We have used first-principles calculations[22,23] to determine the difference in energy between the two structures. Surprisingly, the total calculated difference between the structure models for $Pa\bar{3}$ and $P2_13$ is found to be negligible (ΔE = 48 meV per unit cell), with the centrosymmetric one only slightly lower in energy. However, because the structure refinement does not provide unambiguous support for either space group, we will discuss the features of the crystal structure for simplicity reasons in $Pa\bar{3}$. The atomic positions for both solutions are included in the SI.

The crystal structure (Figure 3a) can be described by a cubic close-packed arrangement of Ba and O (stacking sequence ···ABCA′BCA″BCA···). There are layers containing exclusively O (denoted as B and C). The other types of packing sheets are those of A, A′, or A″ orientation and consist of O and isolated Ba atoms (Figure 3b,c). Accordingly, Ba is found in a cubic octahedral coordination with an average interatomic distance of ≈3.0 Å.

Between these packing layers, Mn and V atoms partially fill the octahedral and tetrahedral voids, respectively. The average interatomic distances Mn–O ≈ 2.18 Å and V–O = 1.73 Å are typical for Mn^{2+} and V^{5+} in their respective coordination spheres; see also Table 2 for selected distances. It should be noted that the coordination sphere around Mn3 contains one hydroxide, leading to a severely distorted polyhedron with angles deviating by ±13° from the orthogonal O–Mn–O arrangement for O_h symmetry, which is closely observed for O–Mn(1,2)–O ($\Delta \approx \pm 1°$).

Table 2. Selected Interatomic Distances (Å) and O^{donor}–H···$O^{acceptor}$ Angles (deg) for $BaMn_9[VO_4]_6(OH)_2$ ($Pa\bar{3}$)

Ba–O11 (×6)	2.857(2)	Mn1–O12 (×3)	2.144(1)
Ba–O12 (×6)	3.165(2)	Mn1–O14 (×3)	2.162(2)
V1–O11	1.679(2)	Mn2–O13 (×6)	2.172(2)
V1–O14	1.721(2)	Mn3–O1	2.119(1)
V1–O12	1.732(2)	Mn3–O11	2.123(2)
V1–O13	1.769(2)	Mn3–O13	2.167(1)
O1–H1	0.95	Mn3–O14	2.176(2)
H1···O14	2.46	Mn3–O12	2.204(2)
O1···O14 (×3)	3.179(3)	Mn3–O13′	2.452(1)
O1–H1···O14	132		

The occupancy of the octahedral and tetrahedral sites for layers adjacent to Ba-containing A-type sheets differs from those between exclusive O-content ones (B and C); see Figure 4. For the former, the sites adjacent to Ba remain unoccupied. Thereby, fragments of edge-connected $[Mn(1,3)O_6]$ polyhedra occur, 25% occupancy of the octahedral sites, with Mn1–Mn3 distances of 3.05 Å. These entities connect further via corners to $[VO_4]$ units, which provide a bridge to seemingly isolated Mn3 octahedra. Only O11 exclusively connects to Mn3 in a terminal position. On the other hand, connectivity between all Mn atoms is found for layers between B and C with 50% occupancy of the octahedral sites. Here, two different surroundings around Mn2 are found: an isolated one separated through exclusive connectivity to vanadates and the other one involving edge-sharing to Mn3. The Mn2–Mn3 distances for connected octahedra are 3.22 Å. Overall, a three-dimensional complicated network of edge-shared $[MnO_6]$ octahedra is formed.

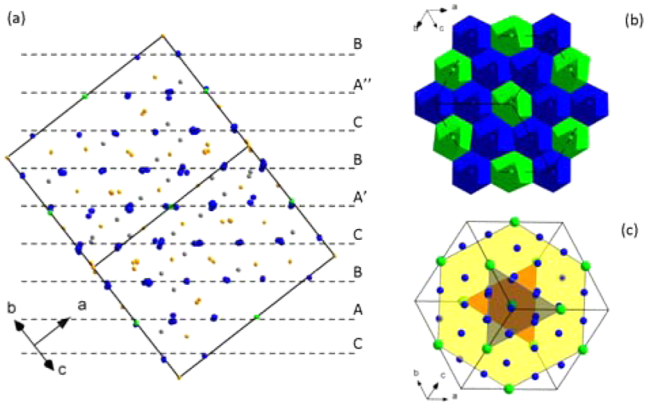

Figure 3. (a) Unit cell with atoms drawn as ellipsoids of 90% probability. (b) Close-packing arrangement (Ba/O): polyhedra for layer A′ central atoms are depicted. Color scheme: Ba, green; Mn, orange; V, gray. H atoms are not shown here. (c) A (red), A′ (yellow), and A″ (gray) packing layers in a projection featuring the difference in the Ba/O distribution.

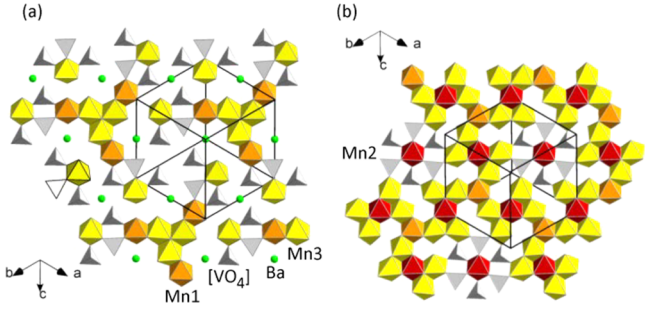

Figure 4. Occupancy of the octahedral (Mn) and tetrahedral (V) sites in $BaMn_9[VO_4]_6(OH)_2$ adjacent to (a) A-type layers and (b) pure O packing layers of the B and C types.

dx.doi.org/10.1021/ic502266k | *Inorg. Chem.* 2015, 54, 898–904

Two interesting structural features are found for the Mn/O part of the structure (Figure 5). The first one is the centered

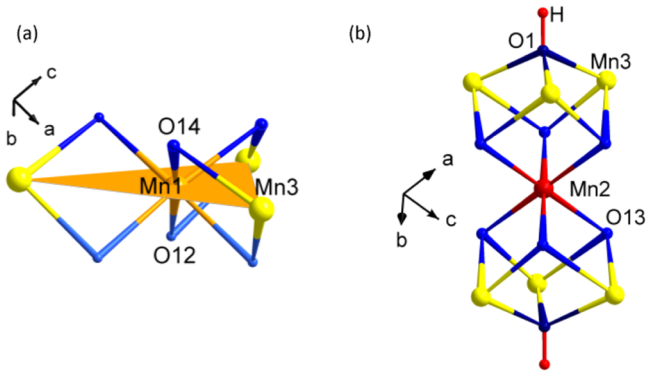

Figure 5. Two features of Mn−O−Mn connectivity: (a) centered triangle; (b) double cube.

isolated triangle Mn1−$Mn3_3$, which is linked exclusively by O atoms provided by the vanadate. The second feature is a double cube consisting of O-bridged $Mn3_3$−Mn2−$Mn3_3$ entities. Again, the connectivity Mn2−Mn3 involves only O from the $[VO_4]$ unit. The end-on feature is the OH^- group capping three Mn3 atoms.

IR and RA Spectroscopy. In Figures 6 and 7, the IR and RA spectra are shown. Stretching vibrations, ν, occur around 400

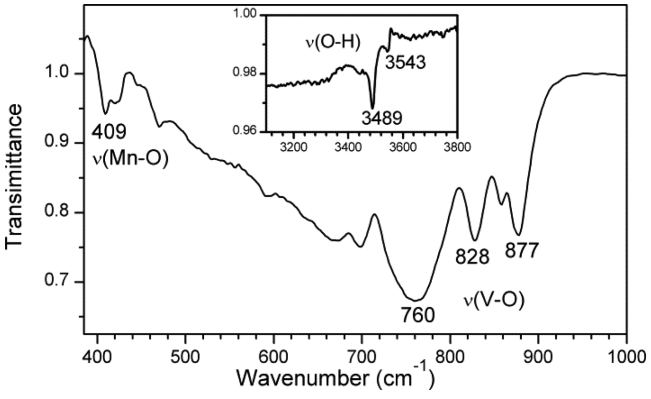

Figure 6. Main panel: Powder IR spectrum for $BaMn_9[VO_4]_6(OH)_2$ in the spectral region of Mn−O and V−O stretching vibrations, ν. Inset: In-phase and out-of-phase O−H modes.

cm^{-1} for Mn−O, at 700−900 cm^{-1} for V−O, and around 3500 cm^{-1} for O−H. A $[VO_4]^{3-}$ complex is expected to exhibit four fundamental stretching modes, which should be both IR- and RA-active for the present case of C_1 symmetry.[25] The highest intensity mode at 804 cm^{-1} (RA) is not observed in the IR spectrum and thus is assigned to the symmetric V−O stretching. The modes at 760 and ≈878 cm^{-1} occur in the IR (strong) and RA (weak) spectra. The latter mode has RA intensity only in cross-polarization (HV). The 866 cm^{-1} mode is seen in the IR spectrum as a weak shoulder and exhibits moderate polarization in the RA spectrum. Thus, we assign the three latter modes to predominantly asymmetric V−O stretching vibrations. The mode at ≈322 cm^{-1} relates to the bending vibrations of the vanadate and can be seen in the RA spectrum. Around 200 cm^{-1}, a lattice mode is clearly visible. Overall, the RA-mode frequencies are in excellent agreement with the nonpolarized RA spectrum reported earlier for the mineral nabiasite.[9]

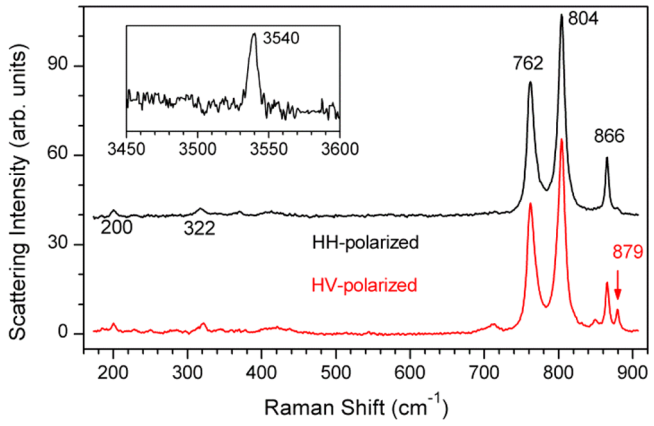

Figure 7. Main panel: Single-crystal RA spectrum for $BaMn_9[VO_4]_6(OH)_2$ for parallel (HH) and crossed (HV) polarizations of incident and scattered light. Inset: In-phase O−H mode.

The vibrations of the hydroxide are observed at 3489 and 3543 cm^{-1} in the IR spectra. Similar values have been reported for volborthite, $Cu_3V_2O_7(OH)_2{\cdot}2H_2O$.[26] The red shift of the stronger IR-mode (tentatively assigned to an out-of-phase displacement) is often taken as an indicator for hydrogen bonding.[27] In comparison, typical "free" OH^- ions exhibit vibrations around 3556 cm^{-1}.[28,29] Considering the geometric information (Table 2) and the relative red shift, $\Delta\nu$(O−H) ≈ −67 cm^{-1}, the interaction between the proton of the hydroxide and vanadate is thus weak and dominantly of electrostatic origin. The higher-frequency ν(O−H) mode is detected also in the RA spectrum and consequently assigned to an in-phase displacement.

Magnetic Properties. The inverse susceptibility, $1/\chi(T)$, for $BaMn_9[VO_4]_6(OH)_2$ (Figure 8a) has been fitted to a Curie−

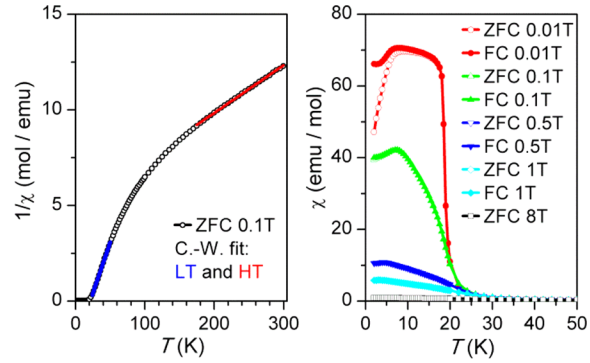

Figure 8. Susceptibility data for $BaMn_9[VO_4]_6(OH)_2$. Left: $1/\chi(T)$ with fits to the Curie−Weiss law. Right: $\chi(T)$ data at various fields in the fc and zfc modes.

Weiss law above 175 K. The Curie constant C^{HT} = 40.11 emu·K/mol is found and indicates an effective moment equivalent to the sum of nine paramagnetic $S = {}^5/_2$ ions per formula unit (calcd 39.39 emu·K/mol). The Weiss temperature $\Theta^{HT} \approx -195$ K points toward strong antiferromagnetic interactions. The absence of an anomaly in the high-temperature (HT) region at around ≈200 K is taken as a confirmation for the presence of antiferromagnetic short-range order. Below 150 K, a gradual change is observed in $1/\chi(T)$. Fitting the low-temperature (LT) range (50−25 K) gives C^{LT} = 9.437 emu·K/mol ($\approx 2S^{5/2}$) and $\Theta^{LT} \approx 20$ K. The positive intersection with the temperature axis

dx.doi.org/10.1021/ic502266k | Inorg. Chem. 2015, 54, 898−904

indicates onset of ferromagnetic types of interactions, leading to long-range order at $T_C \approx 20$ K. Thus, $BaMn_9[VO_4]_6(OH)_2$ can be classified as a ferrimagnet or a canted antiferromagnet.

Figure 8b shows the $\chi(T)$ data in the LT range for fields up to 8 T in the fc and zfc modes. At low fields (H = 0.01 T), splitting occurs between zfc and fc data below 10 K. At around 7.5 K, a kink is observed for the 0.1 T data and the zfc/fc splitting vanishes. This kink feature shifts to lower temperatures upon applied fields and thus should be assigned to an increasing contribution of antiferromagnetic correlations. Hence, we find evidence for competing antiferromagnetic and ferromagnetic interactions at low temperatures.

In Figure 9, we present the $\chi T(T)$ data along with magnetization. The dip around 70 K in $\chi T(T)$ indicates the

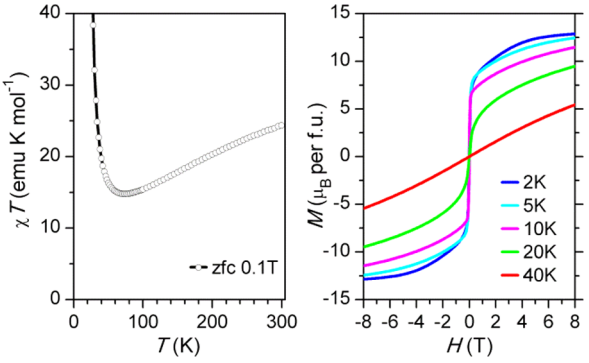

Figure 9. $\chi T(T)$ (left) and $M(H)$ data for $BaMn_9[VO_4]_6(OH)_2$.

crossover between dominantly antiferromagnetic and the onset of ferromagnetic correlations. The value of χT at 70 K amounts to ≈14.7 emu·K/mol, which is close to $^1/_3$ of the paramagnetic value for all nine Mn^{2+} and thus suggests an effective spin system of $S^{eff} = {}^{15}/_2$ (calcd 13.1 emu·K/mol) at lower temperatures. The magnetization measurements, $M(H)$, reveal strong antiferromagnic correlations above T_C (see data for 40 K), as suggested by the linear slope and the effectivly reduced magnetic moment. Below T_C, a steep increase upon applied fields is evident and indicates the onset of predominantly ferromagnetic interations. The inflection point occurs at ≈0.15 T (2 K data), and the magnetic moment changes gradually from ≈7 to ≈12.7 μ_B upon applied fields, reaching a plateau above 4 T. At the highest field measured, approximately $^1/_3$ of the expected saturated moment ($M_S = 9 \times 5\ \mu_B$) is reached, again indicating that the magnetic properties of $BaMn_9[VO_4]_6(OH)_2$ can be attributed to an effective spin system, $S^{eff} = {}^{15}/_2$, below 50 K. The reduction from the expected value of 15 μ_B at LT, furthermore, suggests that competing antiferromagnetic correlations exist. Thus, we suggest that frustration phenomena should be accounted for in the canted antiferromagnetic ground state of $BaMn_9[VO_4]_6(OH)_2$.

Specific Heat. The measured specific heat, $C_p(T)$, for $BaMn_9[VO_4]_6(OH)_2$ in zero applied field is given in Figure 10a. At low temperatures, an anomaly occurs at T_C = 18.3 K (H = 0 T), which broadens and then quickly vanishes upon applied fields (Figure 10b). The associated heat of the anomaly shifts to higher temperatures upon increasing fields and confirms the origin of the magnetic interaction being of a ferromagnetic nature. Another puzzling feature of the $C_p(T)/T$ data is the additional contribution occurring below 10 K with a maximum of around 3 K. Upon increasing fields (above $H \approx 0.1$ T), this feature decreases, smears out, and adds to the broad hump at higher temperatures. Note that above 50 K all measurements follow the

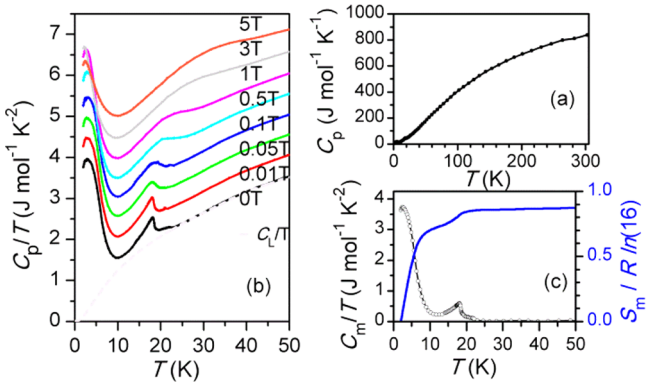

Figure 10. Specific heat data for $BaMn_9[VO_4]_6(OH)_2$. (a) Total specific heat at zero field. (b) Low temperature $C_p(T)/T$ data for various applied fields (data offset: 0.5 J/mol·K^2 per increasing applied field). The dashed line represents the fitted lattice contribution, $C_L(T)/T$. (c) Magnetic part of the specific heat, $C_m(T)/T$, at zero fields (black) and the associated entropy, $S_m(T)$ (blue).

temperature dependence of the zero-field measurement. Thus, the magnetic part of the specific heat below 50 K is constant for all fields measured and subject to significant fluctuations.

In Figure 10c, we show the magnetic part of the specific heat, $C_m(T)$, and the associated magnetic entropy, $S_m(T)$. In a first approximation, we neglect the short-range magnetic contributions associated with the HT region because they are expected to range well beyond 300 K. Accordingly, a (reduced) lattice part of the specific heat, $C_L(T)$, can be obtained from fitting a baseline to the temperature region from 30 to 300 K. We extrapolated the HT fit to ≈10 K and adjusted the approach toward 0 K by the Debye law, $C_L(T)^{LT} = bT^3$. $C_m(T)$ data are then obtained by subtracting $C_L(T)$ from $C_p(T)$. Integrating $C_m(T)/T$ gives the magnetic part of the entropy released in the temperature range from 2 to 50 K. Note that we give S_m in units of R (gas constant) and $\ln(2S^{eff} + 1)$, with $S^{eff} = {}^{15}/_2$; see also above. Overall, we find approximately 90% of the associated magnetic entropy released, which corroborates the results from the susceptibility data. At around 10 K (≈70%), a plateau in $S_m(T)$ separates the low-temperature feature from the area of the anomaly (≈20%).

Dielectric Measurements. In Figure 11, we show the measured dielectric constant, $\varepsilon(T)$, for $BaMn_9[VO_4]_6(OH)_2$ at temperatures below 50 K. The dielectric constant initially decreases to ≈37 K, which is a common T-dependent behavior

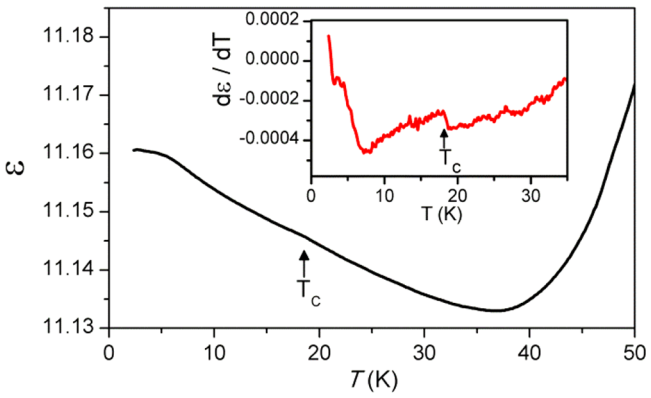

Figure 11. Main panel: Temperature dependence of the dielectric constant for $BaMn_9[VO_4]_6(OH)_2$. Inset: Derivative of the dielectric constant indicating an anomaly at T_C.

dx.doi.org/10.1021/ic502266k | Inorg. Chem. 2015, 54, 898−904

for oxides. However, upon further lowering of the temperature, $\varepsilon(T)$ starts to increase again. At the order transition, $T_C \approx 18$ K, a kink is observed; see also the derivative plot shown in the inset of Figure 11. The change in the dielectric constant at the magnetic ordering temperature (magnetodielectric effect) is frequently observed at magnetic transitions due to spin−lattice coupling. Polarization measurements have not been conducted because of the small crystal sizes. Thus, a ferroic classification of the magnetopolarization coupling type cannot be confirmed here.[1] Below ≈10 K, the increase in $\varepsilon(T)$ slows down and develops into a plateau; see $d\varepsilon(T)/dT$. It is interesting to note that $C_m(T)$ shows the development of a LT feature with a maximum of around 3 K in the same temperature range. One might speculate that the magnetic fluctuations evident from the magnetic specific heat and dielectric constant are coupled. Certainly, these initial characteristics suggest that $BaMn_9[VO_4]_6(OH)_2$ presents a rather interesting and unique case, which calls for further experimental studies and a theoretical microscopic picture.

DISCUSSION

Here, we present a model for the evaluated thermodynamic data. We propose that at high temperatures short-range antiferromagnetic correlations are dominant. These are associated with the centered triangle feature; see Figure 5a. The ground state of this entity is represented by a $S^{c\text{-}T} = {}^{10}/_{2}$ spin system and originates from an antiparallel arrangement of the spherical ions, 3 × Mn3, with the center ion, Mn1.[30] Thus, the three Mn3 moments are forced into a parallel orientation. This fragment has received considerable attention in the field of single-molecule magnets.[31,32]

Further connectivity of three Mn3, being members of independent centered triangles, results in the formation of a triangle. Two $Mn3_3$ triangles are located above and below Mn2; see Figure 5b. Such an equilateral triangle of magnetic ions represents a geometrically frustrated case for dominating antiferromagnetic interactions. Adding to this frustrated feature is the angle of the magnetic moments per Mn3 as induced by the orientation of the centered triangle in space; see the "paddle-wheel" structure depicted in Figure 12. For the centrosymmetric case ($Pa\bar{3}$), a spiral arrangement results with canting in an out-of-plane fashion on each $Mn3_3$ triangle (Figure 12a). Note that inversion symmetry forces the out-of-plane orientation of Mn3 moments per triangle opposing each other. Thus, it is impossible to align the central Mn2 moment antiparallel to both $Mn3_3$ triangles.

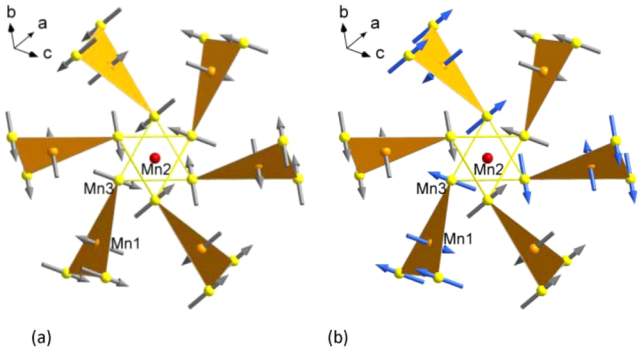

Figure 12. Sketch of the proposed chiral spin arrangement for the centrosymmetric (a) and acentric (b) cases. Note the inverted spin alignment (blue arrows) for the latter one.

Breaking of the inversion symmetry ($P2_13$) allows for an arrangement of all out-of-plane canted moments on the two adjacent $Mn3_3$ triangles pointing in the same direction (Figure 12b). Thus, an antiferromagnetic scenario involving Mn2 with the six Mn3 ions might occur; compare also to Figure 5b. However, the canting of the in-plane Mn3 moments per triangle cannot be resolved through symmetry reduction and remains chiral.

Overall, the compound consists of nine Mn^{2+} ions, each with $S = {}^{5}/_{2}$. If we count the two Mn1 and one Mn2 per formula unit as antiferromagnetically coupled to the six Mn3 ions, an effective spin of $S^{eff} = {}^{15}/_{2}$ results. Alternatively, one derives the same S^{eff} value by ${}^{6}/_{3}S^{c\text{-}T} - S^{5/2} = {}^{15}/_{2}$. Our data indeed show that this effective spin system is present below 50 K. Strong fluctuations persist down to low temperatures, which are presumably caused by the frustrated nature of the Mn3−Mn3 interaction on the triangle. The helical nature of the additional canting adds to the development of the ferromagnetic feature observed in the magnetic and specific heat data at T_C.

CONCLUSIONS

We have redetermined the crystal structure of $BaMn_9[VO_4]_6(OH)_2$ and found signs for a possible acentric structure, as indicated by violations of the diffraction selection rules (single-crystal data) and intensity differences for the refined powder X-ray patterns. The report on the naturally occurring mineral nabiasite, $BaMn_9[(V,As)O_4]_6(OH)_2$, includes a comment on grains (≈10−20 μm size) that are found to be anisotropic under polarized light, which should not be observed for the space group $Pa\bar{3}$.[9] In Figure 1, we show that this is also observed for the synthetic compound presented here. In a cubic system, the space groups of class 23 contain four polar axes along ⟨111⟩. Hence, optical activity and piezoelectricity may occur but not pyroelectricity.[23] However, on the basis of the evaluation of interatomic distances and angles, it seems unlikely that the structure should be acentric as a result of "chemical" strain effects. Instead, we suggest that magnetic correlations induce symmetry breaking. On the basis of these considerations, the structure solution in $P2_13$ appears to be more favorable with respect to $Pa\bar{3}$.

Furthermore, we presented dielectric constant measurements to provide evidence for the magnetodielectric coupling of magnetic long-range order to the lattice around T_C. It would be interesting to study the structure below the transition temperature to probe for further symmetry reduction to the non-isomorphous subgroup, space group $R3$ (No. 146), which would allow for the occurrence of pyroelectricity, a necessary requirement for the occurrence of multiferroicity.

On the basis of the rather complicated connectivity of selected structural features, we propose a scenario for the competing antiferromagnetic and ferromagnetic correlations present for this presumably frustrated and canted antiferromagnet. Further neutron diffraction data are warranted to confirm our model and elucidate the magnetic structures also in applied magnetic fields. Overall, the T−H phase diagram should be quite unique because of the expected richness of magnetic phases with intriguing degenerate ground states. Finally, we point out that, due to the competing antiferromagnetic and ferromagnetic interactions presumably stabilizing chirality, this compound might be a novel candidate for a skyrmion-type lattice.

dx.doi.org/10.1021/ic502266k | Inorg. Chem. 2015, 54, 898−904

■ ASSOCIATED CONTENT

Supporting Information

X-ray crystallographic data in CIF format, atomic positions, and a comparison of selected interatomic distances and angles for the structure solutions ($P2_13$ and $Pa\bar{3}$). This material is available free of charge via the Internet at http://pubs.acs.org. Further details of the crystal structure investigations may be obtained from Fachinformationszentrum Karlsruhe, 76344 Eggenstein-Leopoldshafen, Germany [fax (+49)7247-808-666; e-mail crysdata@fiz-karlsruhe.de; website http://www.fiz-karlsruhe.de/request_for_deposited_data.html) on quoting the CSD number 428505 or 428506.

■ AUTHOR INFORMATION

Corresponding Author

*E-mail: amoeller@uh.edu.

Author Contributions

The manuscript was written through contributions of all authors.

Notes

The authors declare no competing financial interest.

■ ACKNOWLEDGMENTS

This work was supported by the National Science Foundation (Grant DMR-1149899) and by the State of Texas through the Texas Center for Superconductivity at the University of Houston.

■ REFERENCES

(1) (a) Eerenstein, W.; Mathur, N. D.; Scott, J. F. *Nature* **2006**, *442*, 759−765. (b) Cheong, S.-W.; Mostovoy, M. *Nature* **2007**, *6*, 13−20.

(2) Tokura, Y.; Seki, S. *Adv. Mater.* **2010**, *22*, 1554−1565.

(3) Tokura, Y.; Seki, S.; Nagaosa, N. *Rep. Prog. Phys.* **2014**, *77*, 076501.

(4) Johnson, R. D.; Radaelli, P. G. *Annu. Rev. Mater. Res.* **2014**, *44*, 269−98.

(5) (a) Singh, K.; Caignaert, V.; Chapon, L.; Pralong, V.; Raveau, B.; Maignan, A. *Phys. Rev. B* **2012**, *86*, 024410. (b) Caignaert, V.; Maignan, A.; Singh, K.; Simon, C.; Pralong, V.; Raveau, B.; Mitchell, J.; Zheng, H.; Huq, A.; Chapon, L. *Phys. Rev. B* **2013**, *88*, 174403.

(6) (a) Kenzelmann, M.; Lawes, G.; Harris, A. B.; Gasparovic, G.; Broholm, C.; Ramirez, A. P.; Jorge, G. A.; Jaime, M.; Park, S.; Huang, Q.; Shapiro, A. Ya.; Demianets, L. A. *Phys. Rev. Lett.* **2007**, *98*, 267205. (b) White, J. S.; Niedermayer, Ch.; Gasparovic, G.; Broholm, C.; Park, J. M. S.; Shapiro, A. Ya.; Demianets, L. A.; Kenzelmann, M. *Phys. Rev. B* **2013**, *88*, 060409(R).

(7) Amuneke, N. E.; Tapp, J.; de la Cruz, C. R.; Möller, A. *Chem. Mater.* **2014**, *26*, 5930−5935.

(8) (a) Seki, S.; Yu, X.; Ishiwata, S.; Tokura, Y. *Science* **2012**, *336*, 198−201. (b) Adams, T.; Chacon, A.; Wagner, M.; Bauer, A.; Brandl, G.; Pedersen, B.; Berger, H.; Lemmens, P.; Pfeiderer, C. *Phys. Rev. Lett.* **2012**, *108*, 237204. (c) Mochizuki, M.; Yu, X. Z.; Seki, S.; Kanazawa, N.; Koshibae, W.; Zang, J.; Mostovoy, M.; Tokura, Y.; Nagaosa, N. *Nat. Mater.* **2014**, *13*, 241.

(9) Bruggeru, J.; Bonin, M.; Schenk, K. J.; Meisser, N.; Berlepsch, P.; Ragu, A. *Eur. J. Mineral.* **1999**, *11*, 879−890.

(10) (a) von Postel, M.; Müller-Buschbaum, Hk. *Z. Anorg. Allg. Chem.* **1992**, *615*, 97−100. (b) He, Z.; Ueda, Y.; Itoh, M. *Solid State Commun.* **2007**, *141*, 22−24.

(11) (a) Rettich, R.; Müller-Buschbaum, Hk. *Z. Naturforsch.* **1998**, *53b*, 291−295. (b) Bratsch, M.; Tapp, J.; Litvinchuk, A. P.; Möller, A. *Inorg. Chem.* **2014**, *53*, 4994−5001.

(12) Zhang, F.; Zavalij, P. Y.; Whittingham, M. S. *J. Mater. Chem.* **1999**, *9*, 3137−3140.

(13) Sun, K.; Möller, A. *Acta Crystallogr., Sect. E* **2014**, *70*, i33.

(14) Kolitsch, U. *Acta Crystallogr., Sect. E* **2001**, *57*, i119−i121.

(15) (a) Zhang, G.; Dong, S.; Yan, Z.; Guo, Y.; Zhang, Q.; Yunoki, S.; Dagotto, E.; Liu, J.-M. *Phys. Rev. B* **2011**, *84*, 174413. (b) Johnson, R. D.; Chapon, L. C.; Khalyavin, D. D.; Manuel, P.; Radaelli, P. G.; Martin, C. *Phys. Rev. Lett.* **2012**, *108*, 067201.

(16) *SAINT*, version 7.60A; Bruker AXS Inc.: Madison, WI, 2002−2014.

(17) Sheldrick, G. M. *Acta Crystallogr., Sect. A* **2008**, *64*, 112−122.

(18) Blessing, R. H. *Acta Crystallogr., Sect. A* **1995**, *51*, 33−38.

(19) *WinGX*, version 2013.3: Farrugia, L. J. *J. Appl. Crystallogr.* **2012**, *45*, 849−854.

(20) Brandenburg, K. *Diamond*, version 3.2i; Crystal Impact GbR: Bonn, Germany, 1997−2012.

(21) Rodriguez-Cavajal, J. *Program FullProf*, version 2.05; Laboratoire Léon Brillouin CEA-CNRS: Gif-sur-Yvette, Cedex, France, 2011.

(22) Perdew, J. P.; Burke, K.; Ernzerhof, M. *Phys. Rev. Lett.* **1996**, *77*, 3865−3568.

(23) Clark, S. J.; Segall, M. D.; Pickard, C. J.; Hasnip, P. J.; Probert, M. J.; Refson, K.; Payne, M. C. *Z. Kristallogr.* **2005**, *220*, 567−570.

(24) Spek, A. L. *Acta Crystallogr., Sect. D* **2009**, *65*, 148−155.

(25) Nakamoto, K. *Infrared and Raman Spectra of Inorganic and Coordination Compounds, Part A, Theory and Applications in Inorganic Chemistry*, 6th ed.; Wiley: New York, 2009.

(26) Frost, R. L.; Palmer, S. J.; Čejka, J.; Sejkora, J.; Plášil, J.; Bahfenne, S.; Keeffe, E. C. *J. Raman Spectrosc.* **2011**, *42*, 1701−1710.

(27) Steiner, T. *Angew. Chem., Int. Ed.* **2002**, *41*, 48−76.

(28) (a) Beckenkamp, K.; Lutz, H. D. *J. Mol. Struct.* **1992**, *270*, 393−405. (b) Lutz, H. D. *Struct. Bonding (Berlin)* **1995**, *82*, 85−103.

(29) Gheorghe, D. E.; Litvinchuk, A. P.; Möller, A. *Z. Anorg. Allg. Chem.* **2012**, *638*, 2087−2092.

(30) Kahn, O. *Molecular Magnetism*; VCH Publishers, Inc.: New York, 1993.

(31) (a) Barra, A. L.; Caneschi, A.; Cornia, A.; Fabrizi de Biani, F.; Gatteschi, D.; Sangregorio, C.; Sessoli, R.; Sorace, L. *J. Am. Chem. Soc.* **1999**, *121*, 5302−5310. (b) Gatteschi, D.; Sessoli, R.; Cornia, A. *Chem. Commun.* **2000**, 725−732. (c) Gao, Q.; Wang, X.; Tapp, J.; Möller, A.; Jacobson, A. J. *Inorg. Chem.* **2013**, *52*, 6610−6616.

(32) Space-Group Symmetry. In *International Tables for Crystallography*, 5th ed.; Hahn, T., Ed.; Springer: Berlin, 2005; Vol. *A*.